Remote Sens. **2015**, *7*, 5495-5510; doi:10.3390/rs70505495

OPEN ACCESS

remote sensing

ISSN 2072-4292

www.mdpi.com/journal/remotesensing

Article

Land Surface Albedo Estimation from Chinese HJ Satellite Data Based on the Direct Estimation Approach

Tao He [1,*], Shunlin Liang [1,2], Dongdong Wang [1], Xiaona Chen [1,2], Dan-Xia Song [1] and Bo Jiang [2]

[1] Department of Geographical Sciences, University of Maryland, College Park, MD 20742, USA; E-Mails: sliang@umd.edu (S.L.); ddwang@umd.edu (D.W.); chenxn@umd.edu (X.C.); dxsong@umd.edu (D.-X.S.)

[2] State Key Laboratory of Remote Sensing Science, School of Geography, Beijing Normal University, Beijing 100875, China; E-Mail: bojiang@bnu.edu.cn

* Author to whom correspondence should be addressed; E-Mail: the@umd.edu; Tel.: +1-301-405-4538; Fax: +1-301-314-9299.

Academic Editors: Ioannis Gitas and Prasad S. Thenkabail

Received: 1 March 2015 / Accepted: 22 April 2015 / Published: 4 May 2015

Abstract: Monitoring surface albedo at medium-to-fine resolution (<100 m) has become increasingly important for medium-to-fine scale applications and coarse-resolution data evaluation. This paper presents a method for estimating surface albedo directly using top-of-atmosphere reflectance. This is the first attempt to derive surface albedo for both snow-free and snow-covered conditions from medium-resolution data with a single approach. We applied this method to the multispectral data from the wide-swath Chinese HuanJing (HJ) satellites at a spatial resolution of 30 m to demonstrate the feasibility of this data for surface albedo monitoring over rapidly changing surfaces. Validation against ground measurements shows that the method is capable of accurately estimating surface albedo over both snow-free and snow-covered surfaces with an overall root mean square error (RMSE) of 0.030 and r-square (R^2) of 0.947. The comparison between HJ albedo estimates and the Moderate Resolution Imaging Spectral Radiometer (MODIS) albedo product suggests that the HJ data and proposed algorithm can generate robust albedo estimates over various land cover types with an RMSE of 0.011–0.014. The accuracy of HJ albedo estimation improves with the increase in view zenith angles, which further demonstrates the unique advantage of wide-swath satellite data in albedo estimation.

Keywords: surface albedo; direct estimation; medium resolution; snow albedo; HJ data

1. Introduction

Surface shortwave albedo, defined as the ratio of the reflected to the incident solar shortwave radiation at the Earth's surface, is one of the key parameters in surface energy budget studies [1–3].

With advancement in the remote sensing techniques over the past several decades, land surface albedo algorithms have been developed for many remote sensing platforms [4,5]. Coarse resolution (>300 m) satellite albedo products have been widely used for climate modeling and weather forecasting purposes. However, their uncertainties remain a critical issue, preventing a refined understanding of anthropogenic effects on global climate change, particularly over middle- to high-latitude winters [4]. Due to the scale differences between satellite pixels and footprints of ground measurements, data at finer spatial resolutions are needed to bridge the gap over heterogeneous landscapes for a better understanding of uncertainties of coarse-resolution products [6,7]. Moreover, there is an increasing need for the availability of medium-resolution surface albedo for applications at medium-to-fine scales (<100 m), including forest management [8–10], agriculture monitoring [11], and urban environment monitoring [12,13].

China launched two HuanJing (HJ) satellites in September 2008, carrying 30-m resolution multispectral optical sensors similar to Landsat but with swaths that were nearly two times larger, with a revisiting frequency of four days, bringing an opportunity of monitoring surface conditions as a supplementary source to the existing satellite products. The radiometric calibration for HJ data [14–16] allows for many quantitative remote sensing applications monitoring vegetation, atmosphere, and water bodies [17–20]. Thanks to their wide swath, HJ sensors observe the Earth's surface with view zenith angles up to 35°, making it possible to obtain some angular information for surface Bidirectional Reflectance Distribution Function (BRDF) retrievals, which is not available from the nadir-viewing Landsat sensors. With high spatial and temporal resolutions, HJ data can serve as a key supplementary source for monitoring the surface radiation budget and calibrating coarse resolution data.

Effects of surface BRDF on the satellite observations are prominent and have been extensively studied [11,21]. Failure to correct these effects could lead to errors up to 60%, which could be deleterious for applications that require accurate and consistent satellite-derived information [11]. To satisfy the need for medium-resolution albedo products, efforts have been made to derive surface albedo utilizing space-borne and airborne sensors [6,22–24]. Limited by the low revisiting frequency of medium-resolution data, the temporal composite method developed for coarse-resolution data (e.g., [25]) cannot be applied without enough angular samples of surface BRDF. To overcome this limitation, a few algorithms have been developed through using ancillary information on surface BRDF to normalize the surface reflectance after atmospheric correction to obtain surface albedo, which relies on concurrent high-quality coarse-resolution data and is particularly effective for dense vegetation [23,26]. Particularly for HJ data, Gao *et al.* [27] refined the algorithm originally proposed by Shuai *et al.* [22] using the surface BRDF information from coarse-resolution products and land cover maps to convert surface reflectance to albedo. However, the availability of concurrent high-quality clear-sky coarse-resolution BRDF data significantly limited the application of these methods, particularly over rapidly changing surfaces. In order to estimate surface albedo from Landsat without concurrent coarse-resolution data, Shuai *et al.* [23] proposed an algorithm for forest albedo estimation using a look-up table derived from the Moderate Resolution Imaging Spectroradiometer (MODIS) surface BRDF product [25] relying on

the forest disturbance inventory information, which achieved a low root-mean-square-error (RMSE) of 0.016 (~15%) over six forest sites of AmeriFlux.

Existing algorithms designed for medium-resolution data are mainly limited by the availability of concurrent coarse resolution data or ancillary information used to infer the shape of surface BRDF, which is not ideal for cases with rapidly changing surfaces (e.g., ephemeral snow and harvest) or for cases with lack of high-quality ancillary information. In addition, none of these previous efforts have attempted to estimate surface albedo under snow-covered conditions. A series of approaches that directly link surface albedo with top-of-atmosphere (TOA) observations based on statistical relationships built from radiative transfer simulations can therefore be utilized for broadband albedo estimation using one single multispectral observation under such conditions [24,28,29]. Unlike the methods that rely on the concurrent coarse resolution data, this type of approach treats the surface BRDF as a priori knowledge in the radiative transfer simulations; this surface BRDF information can be extracted and synthesized into a database from the MODIS data [25]. This type of approach has been successfully applied to coarse-resolution data; however, it has never been attempted or validated using medium-resolution data.

The main objective of this study is to demonstrate the feasibility of the HJ satellite charge-coupled device (CCD) data to be used for albedo monitoring under various surface conditions based on the direct estimation approach adopted and refined from Wang *et al.* [29] and a surface BRDF database extracted from MODIS products. In this paper, brief introductions of HJ data as well as the methodology are given in Section 2, followed by an analysis of validation against ground measurements and MODIS albedo product in Section 3.

2. Data and Method

2.1. Chinese HJ Satellite Data

On 6 September 2008, China launched two HJ satellites, namely HJ-1A and HJ-1B, each consisting of two CCD cameras. Each CCD camera has a swath of ~360 km with four spectral bands (Table 1) similar to the spectral bands of Landsat data in the visible and near-infrared range. With a total of four wide-swath CCD cameras onboard the HJ satellite constellation, the revisiting frequency is reduced to four days. However, to conserve power the HJ data is mainly collected over China. For other regions, the cameras are programmed to obtain data at different time periods according to specific needs. The Level 2 HJ data were used in this study with radiometric calibration and systematic geometric correction, which were processed and distributed by the China Centre for Resources Satellite Data and Application (CRESDA). The Level 2 data is projected to the Universal Transverse Mercator (UTM) projection. Digital numbers and radiometric calibration coefficients are provided in the data for the calculation of TOA reflectance. The radiometric calibration accuracy is about 5%–8% with respect to Landsat data [14]. In this study, about 130 scenes of HJ data obtained during 2009–2014 were collected from CRESDA with satellite overpass ground stations within the US for validation purposes.

Due to the lack of accurate ground control points outside China, the Level 2 data suffer from georegistration errors up to a few kilometers, particularly for the data acquired by the two CCDs onboard HJ-1B satellite. Manual georeferencing was carried out on all the data to make sure the pixel level geolocations reach an error within ±30 m.

Table 1. Spectral bands (0.4–0.9 μm) of HJ CCD cameras and MODIS.

HJ CCD		MODIS	
Band No.	**Spectral Range (μm)**	**Band No.**	**Spectral Range (μm)**
1	0.43–0.52	3	0.46–0.48
2	0.52–0.60	4	0.55–0.57
3	0.63–0.69	1	0.62–0.67
4	0.76–0.90	2	0.84–0.88

2.2. MODIS Surface BRDF Products

Surface BRDF information has been available from the MODIS sensors onboard Terra and Aqua satellites since the year 2000. The basic principle of the MODIS algorithm is that by collecting the atmospherically corrected surface reflectance within a 16-day period the surface BRDF can be determined by the majority of either clear-sky snow-free or snow-covered observations [25,30]. The MODIS products include surface BRDF parameters and the corresponding data quality that can be used for calculating surface white-sky albedo (independent of solar zenith angle) and black-sky albedo for any given solar zenith angle for each of the seven MODIS land bands and three broadbands. The MODIS products are updated every eight days and available at a nominal 500-m spatial resolution globally. In this study, the good quality 500-m surface BRDF parameter products (Collection 5) of the spectral bands and shortwave broadband were used.

2.3. Flux Tower Measurements

Ground measurements of surface upward and downward shortwave radiation are available from the AmeriFlux and Surface Radiation (SURFRAD) networks (Figure 1). Data from AmeriFlux sites are measured and recorded every half hour. SURFRAD sites record data every minute. Ground albedo data from these networks are calculated as the ratio of upward to downward radiation averaged within the ±30 min window of HJ satellite overpass.

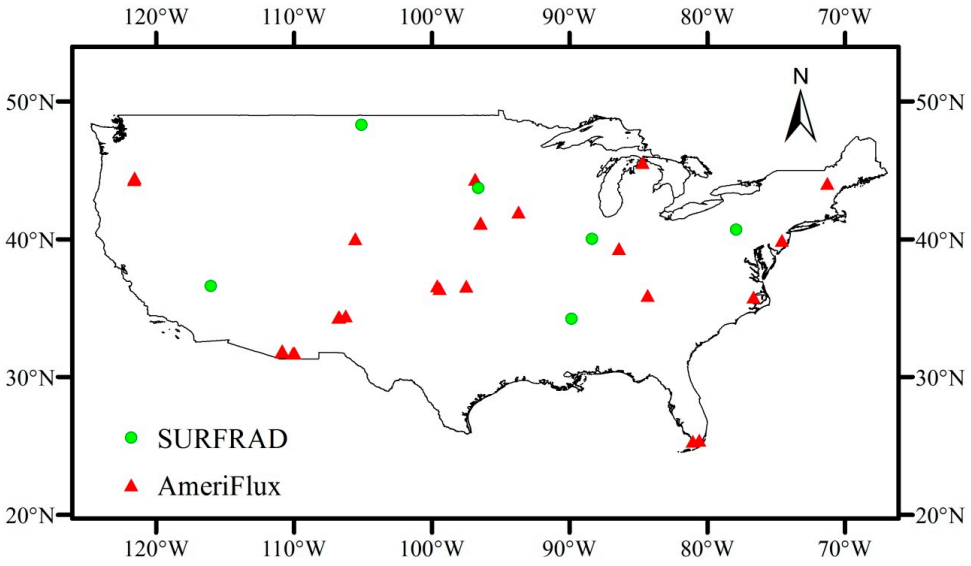

Figure 1. Location of the flux sites from AmeriFlux and SURFRAD networks.

After a cross-check of the HJ data with the ground measurements, clear-sky data from 26 sites in the AmeriFlux network and six SURFRAD sites were included in the validation. These sites cover a variety of land cover types and climate regions.

To match the footprints between the ground measurements and satellite pixels, the actual footprints of the flux towers were calculated, taking into account the instruments' nominal height and field-of-view [31,32].

2.4. Albedo Direct Estimation

The basic principle of albedo direct estimation originated from Liang *et al.* [33] by linking surface broadband albedo (α) with TOA spectral reflectance (ρ_i):

$$\alpha = \sum_{i=1}^{n} \rho_i \cdot c_i + c_0 , \quad (1)$$

where ρ_i is the TOA spectral reflectance for band $i \in [1, n]$, and c_i and c_0 c_0 are regression coefficients as a function of sun-sensor-target geometries.

To establish such statistical relationship, the 6S radiative transfer codes [34] were employed to simulate TOA reflectance under various atmosphere and surface conditions. Configurations of atmospheric conditions and geometries are listed in Table 2.

Table 2. Configurations for simulating surface albedo and TOA reflectance data.

Parameters	Values
Solar zenith angle	0, 5, 10, 15, 20, 25, 30, 35, 40, 45, 50, 55, 60, 65, and 70
View zenith angle	0, 5, 10, 15, 20, 25, 30, and 35
Relative azimuth angle	0, 30, 60, 90, 120, 150, and 180
Aerosol optical depth	0.05, 0.10, 0.15, 0.20, 0.30, 0.40, and 0.60

To account for the effects of surface BRDF on TOA observations, prior knowledge of the surface BRDF is needed as the input to train the statistical relationship, which however is not yet available for the manner of HJ spectral bands. Employing the legacy from the MODIS surface BRDF product [25] can help solve this problem. However, due to the difference in the band design of HJ CCD and MODIS sensors, directly applying MODIS data to HJ bands may lead to errors. A total of 245 surface albedo spectrum samples collected from the US Geological Survey (USGS) and Advanced Spaceborne Thermal Emission and Reflection Radiometer (ASTER) spectral libraries, including samples of vegetation, soil, rock, water, snow, and ice, were used to evaluate the impacts band differences of the two types of sensors on spectral albedo [31]. The surface albedo spectrum data and the sensors' spectral response functions were used to calculate the albedo of the spectral bands through convolution integration.

Figure 2 shows the difference of surface spectral albedos estimated for the two types of sensors. The results demonstrate that errors originated from the band differences are not negligible with RMSEs ranging from 0.007 to 0.021. The errors will propagate into the broadband albedo estimation. Thus, it is necessary to convert the MODIS data to HJ bands considering the band differences.

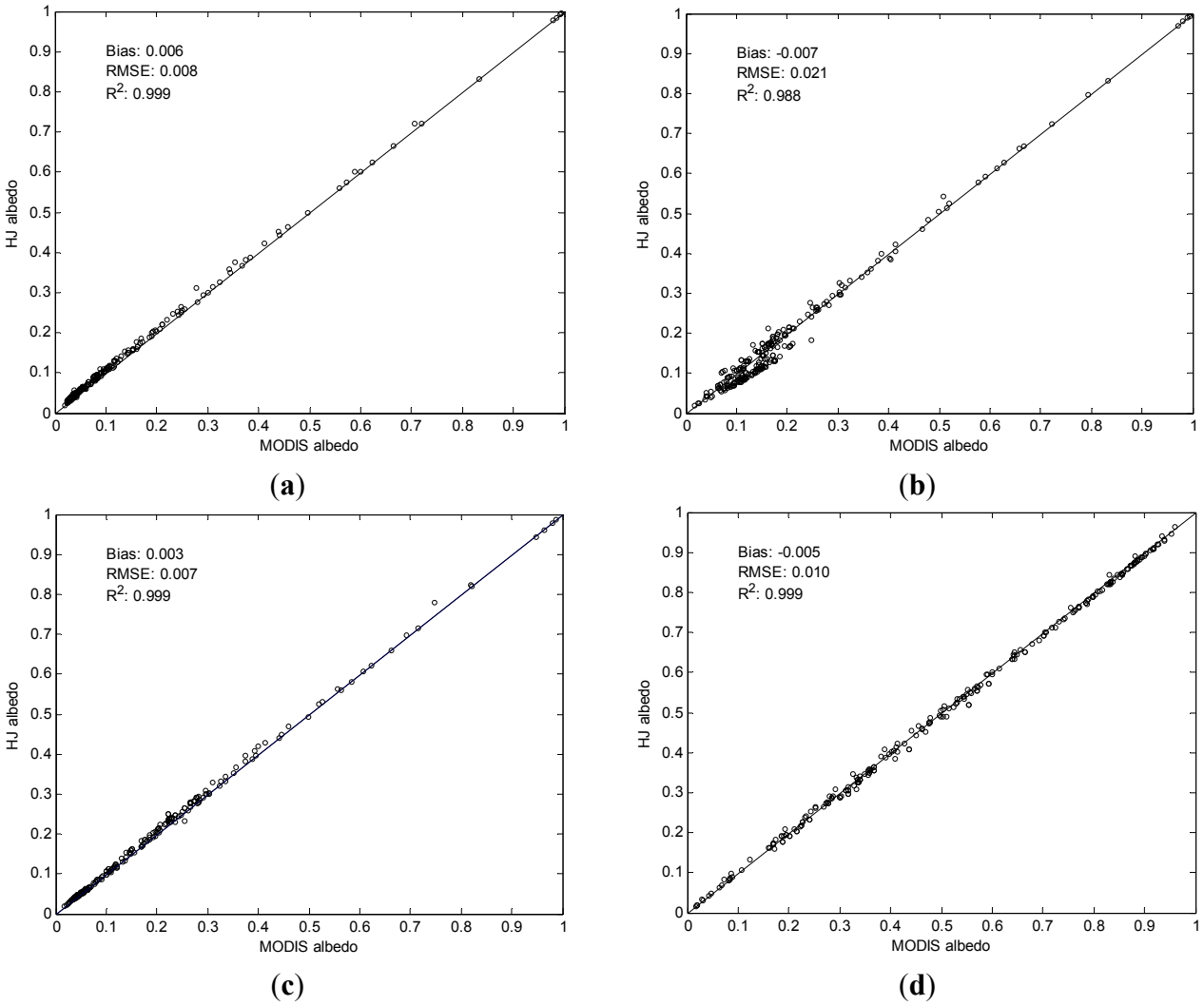

Figure 2. Comparison of spectral albedo integrated using surface albedo spectrum data and sensors' spectral response functions: (**a**) HJ band 1 *vs.* MODIS band 3; (**b**) HJ band 2 *vs.* MODIS band 4; (**c**) HJ band 3 *vs.* MODIS band 1; and (**d**) HJ band 4 *vs.* MODIS band 2. All 245 spectrum samples are included in the scatter plots.

In order to further mitigate the uncertainty in the band conversion process, the other three MODIS land bands were included, namely Band 5 (1.23–1.25 μm), Band 6 (1.63–1.65 μm), and Band 7 (2.11–2.16 μm). The convoluted integrals of HJ spectral albedos were regressed against those of MODIS spectral albedos. Stepwise regression was used for each of the HJ bands to remove unnecessary MODIS bands in the conversion. Linear regression equations are as follows:

$$f_1^H = -0.0087 f_2^M + 0.8764 f_3^M + 0.1313 f_4^M + 0.0050 f_6^M \quad (2)$$

$$f_2^H = 0.2457 f_1^M - 0.0090 f_2^M + 0.0555 f_3^M + 0.7089 f_4^M - 0.0026 f_6^M \quad (3)$$

$$f_3^H = 1.0883 f_1^M - 0.0930 f_4^M + 0.0246 f_6^M - 0.0149 f_7^M \quad (4)$$

$$f_4^H = -0.0386 f_1^M + 1.0190 f_2^M - 0.0339 f_3^M + 0.0861 f_4^M - 0.0564 f_5^M + 0.0225 f_6^M \quad (5)$$

With the help of linear regression, the uncertainties due to band differences (Figure 2) have been significantly reduced with RMSEs ranging from 0.003 to 0.007 (Figure 3). The reason why the linear

regression was used here for band conversion is because of the linear nature of the BRDF kernel model used by MODIS. One thousand high-quality samples of surface BRDF from the MODIS albedo product (MCD43A) were randomly collected over North America for different seasons and land covers including vegetation, soil, and snow samples. Quality checks on the BRDF data were carried out to ensure that only the data flagged with the highest quality were selected and the directional reflectance calculated from the BRDF parameters for all the viewing geometries fell into valid data range [35,36]. Each set of samples contains the spectral and broadband kernel parameters. Having converted the surface kernel parameter data to HJ bands following Equations (2)–(5), radiative transfer simulations were carried out to simulate the HJ TOA reflectances. Surface shortwave broadband albedo was calculated from the broadband kernel parameters with given viewing geometries. Regression coefficients in Equation (1) were estimated based on the simulated TOA reflectance and surface albedo on an angular-bin basis (Table 2), which were then applied directly to the actual HJ TOA reflectances. An example of the linear regression performance based on the simulated data is shown in Figure 4.

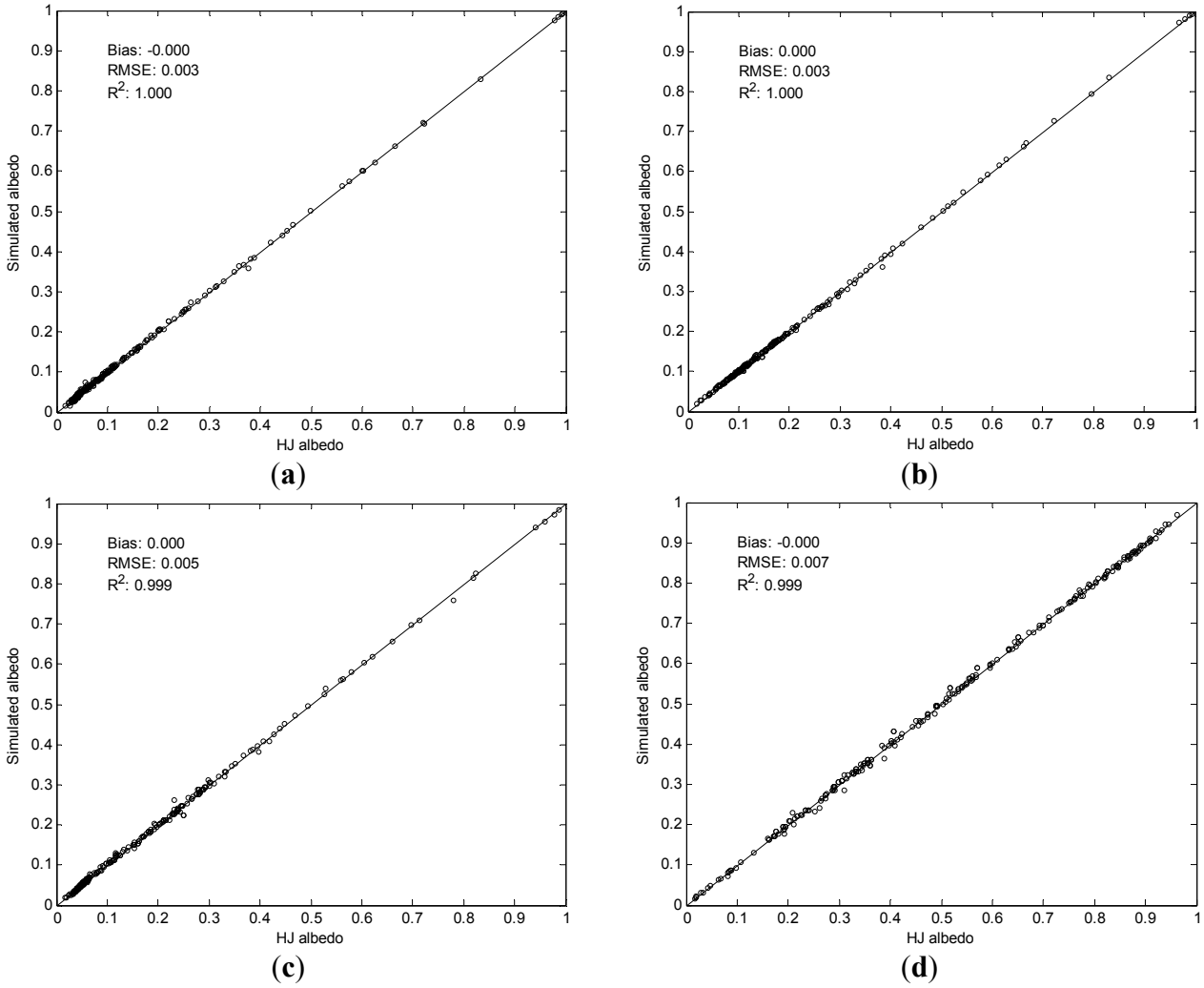

Figure 3. Comparison of HJ spectral albedos and the values estimated from the simulated MODIS spectral albedos using Equations (2)–(5): (**a**) HJ band 1; (**b**) HJ band 2; (**c**) HJ band 3; and (**d**) HJ band 4. All 245 spectrum samples are included in the scatter plots.

The theoretical uncertainties of using HJ TOA reflectance to estimate surface broadband albedo can be constrained within ±0.025, which indicates the feasibility of using HJ TOA reflectance data to estimate surface broadband albedo. The accuracy of black-sky albedo estimation is similar to that of white-sky albedo estimation under the same viewing geometries, which improves with the decrease in solar (view) zenith angle. One interesting finding is that under the same set of solar zenith angle and view zenith angle, angular observations sampled close to the perpendicular plane (relative azimuth angle = 90°) can lead to an improvement in albedo estimation over those sampled close to the principal plane (relative azimuth angle = 0° or 180°), particularly for larger solar zenith angles; however, the improvement is not significant.

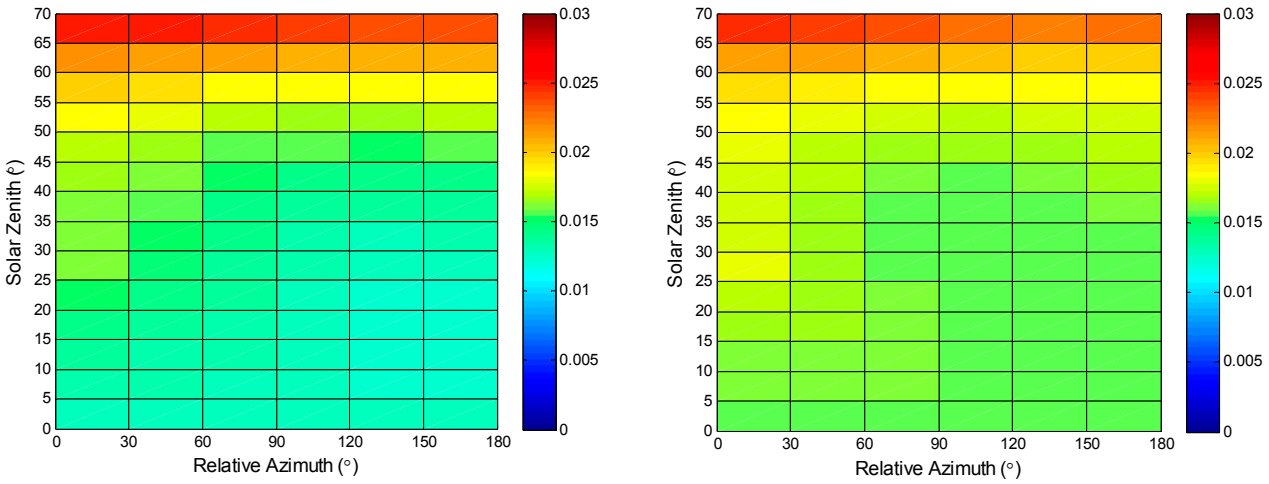

Figure 4. RMSEs of using simulated HJ TOA reflectance (view zenith angle = 25°) to estimate surface broadband shortwave albedos: (**a**) black-sky albedo; and (**b**) white-sky albedo.

3. Results and Discussion

3.1. Validation against Ground Measurements

Validations at AmeriFlux (Figure 5) and SURFRAD (Figure 6) sites were made using all available clear-sky HJ data and ground measurements. Results from both networks show negligible bias (within 0.003) and high determination coefficients (R^2: 0.88–0.98). The RMSEs are well constrained within 0.024–0.033 considering that this approach can also estimate snow-covered albedos. Combining results from the two networks the RMSE and R^2 are 0.030 and 0.947, respectively, for all the cases; while the RMSE and R^2 drop to 0.029 and 0.618, respectively, for snow-free cases. We also found that reducing the resolution of solar zenith angle in the look-up tables (Table 2) to 20° would only cause slightly worse results, with an increase in RMSEs of less than 0.002.

The effects of surface BRDF on the remotely sensed signals were corrected through the incorporation of the BRDF database into the radiative transfer simulations. In Figure 7, the relative estimation errors seem to be randomly distributed with solar zenith angle and view zenith angle, which indicates that the estimation biases do not have any significant relationship with the geometries over various types of land covers. Figure 7 also shows that the absolute errors tend to decrease with the increase in view zenith angle, which demonstrates the potential of improving the albedo estimation from the wide swath HJ data; however, more data are needed before any solid conclusions can be made.

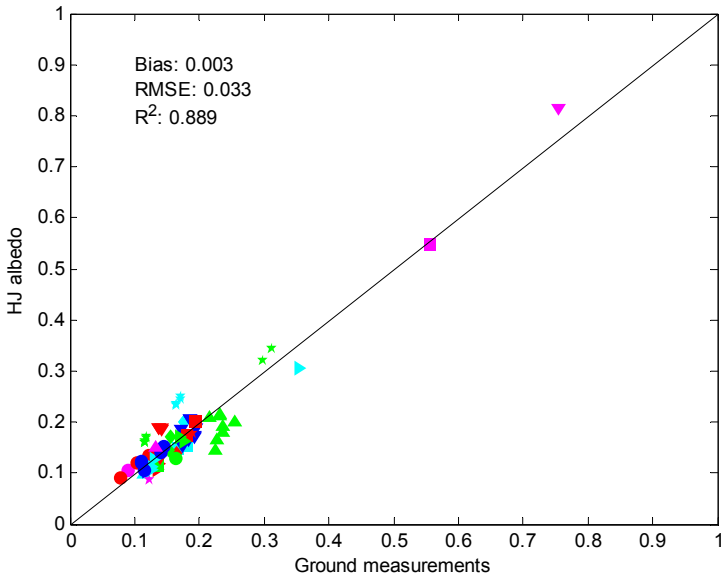

Figure 5. Comparison of HJ shortwave albedo and ground measurements at 26 AmeriFlux sites (n = 74). Different colors and shapes represent different sites.

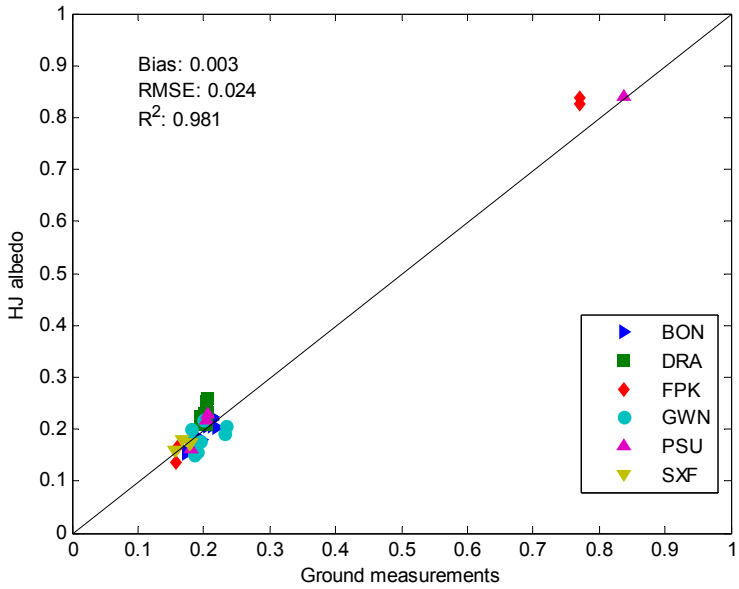

Figure 6. Comparison of HJ shortwave albedo and ground measurements at six SURFRAD sites (n = 49).

Because surface albedo is strongly correlated with land cover type, it is therefore useful to further examine the results by breaking down the validation samples into different land covers, namely forest, grassland/cropland, and open shrub/woody savanna (Table 3). The forest sites observed low surface albedo and often high landscape homogeneity. Thus, surface albedo estimation achieved the lowest bias and RMSE at the forest sites among the three land cover classes. As the vegetation canopy fraction decreases, surface albedo gradually increases. Validation uncertainty of surface albedo can be affected by the increased surface heterogeneity as a result of different combinations of vegetation and background soil fractions. Albedo estimates at the grassland and cropland sites were found to have a slight negative bias of 0.018 compared with the ground measurements. At the same time, an overestimation of 0.022 in albedo is associated with the sparsely-vegetated sites. The validation results shown here agree well with

the finding in an earlier study that focused on MODIS albedo products, which demonstrated the albedo overestimation at woody savanna sites and underestimation at grassland and cropland sites [37].

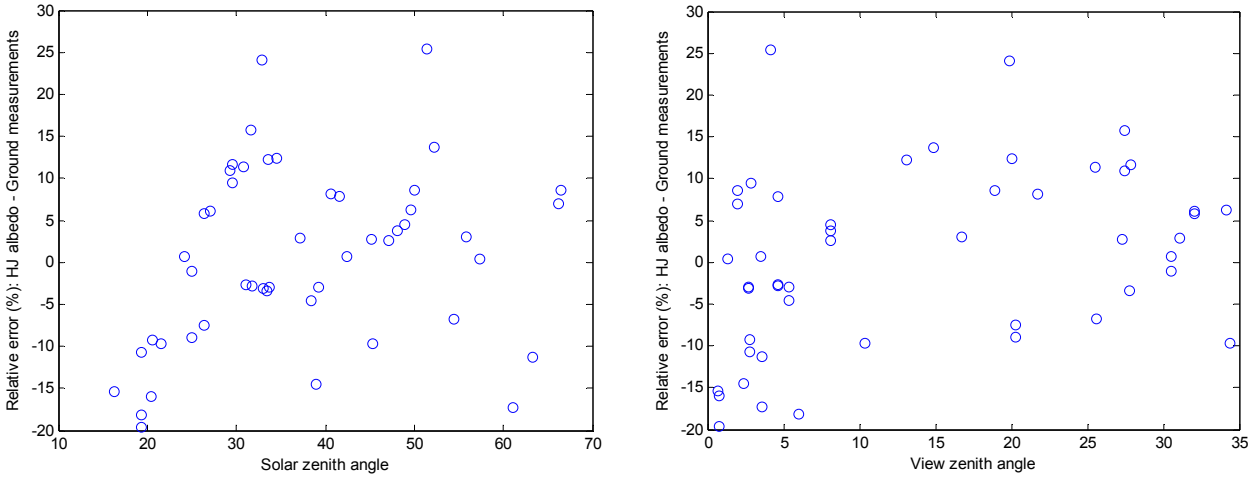

Figure 7. Relationship of relative estimation error in shortwave albedo and sun-sensor-target geometries.

Table 3. Albedo estimation accuracy for different land cover types at Ameriflux sites.

Land Cover *	Mean	Standard Deviation	Bias	RMSE	*N*
DBF-ENF-EBF	0.138	0.045	0.004	0.026	27
GRA-CRO	0.177	0.036	−0.018	0.052	37
OSH-WSV	0.196	0.062	0.022	0.031	13

* ENF: Evergreen needleleaf forest; EBF: Evergreen broadleaf forest; DBF: Deciduous broadleaf forest; OSH: Open shrublands; WSV: Woody savannas; GRA: Grasslands; CRO: Croplands.

3.2. Comparison with MODIS Albedo Product

To further demonstrate the ability of the proposed algorithm using HJ data in albedo estimation, a comparison was made between the albedo maps from HJ data and 500-m MODIS albedo product (MCD43A). Due to the difference in acquisition time of the two satellite series, the white-sky albedo was chosen for comparison, which is theoretically independent of solar zenith angle and thus acquisition time. The black-sky albedo included in MODIS product was generated with solar zenith angle at noon local time; thus, in order to compare the black-sky albedo from HJ data with MODIS product, the black-sky albedo was calculated from MODIS BRDF parameters with the HJ overpass solar zenith angle. Because MODIS albedo products are generated based on a temporal composition approach, their albedo values represent the dominant surface conditions within the 16-day composite window under clear-sky conditions. Thus, the comparison was made for data obtained in later summer to reduce the impact of surface changes as well as covering a variety of land cover types including forest, cropland, grassland, and urban areas (Figure 8).

Manual georegistration was carried out on the scene using the Level 1T Landsat images (standard terrain correction) downloaded from USGS. A second-order polynomial transformation function successfully reduced the geolocation error from kilometers in the original Level 2 HJ data to within ±30 m compared with Landsat data. The MODIS albedo products were reprojected to UTM projection

to match the georegistered HJ data. HJ albedo was then spatially aggregated to MODIS resolution using the mean HJ albedo value within a MODIS pixel.

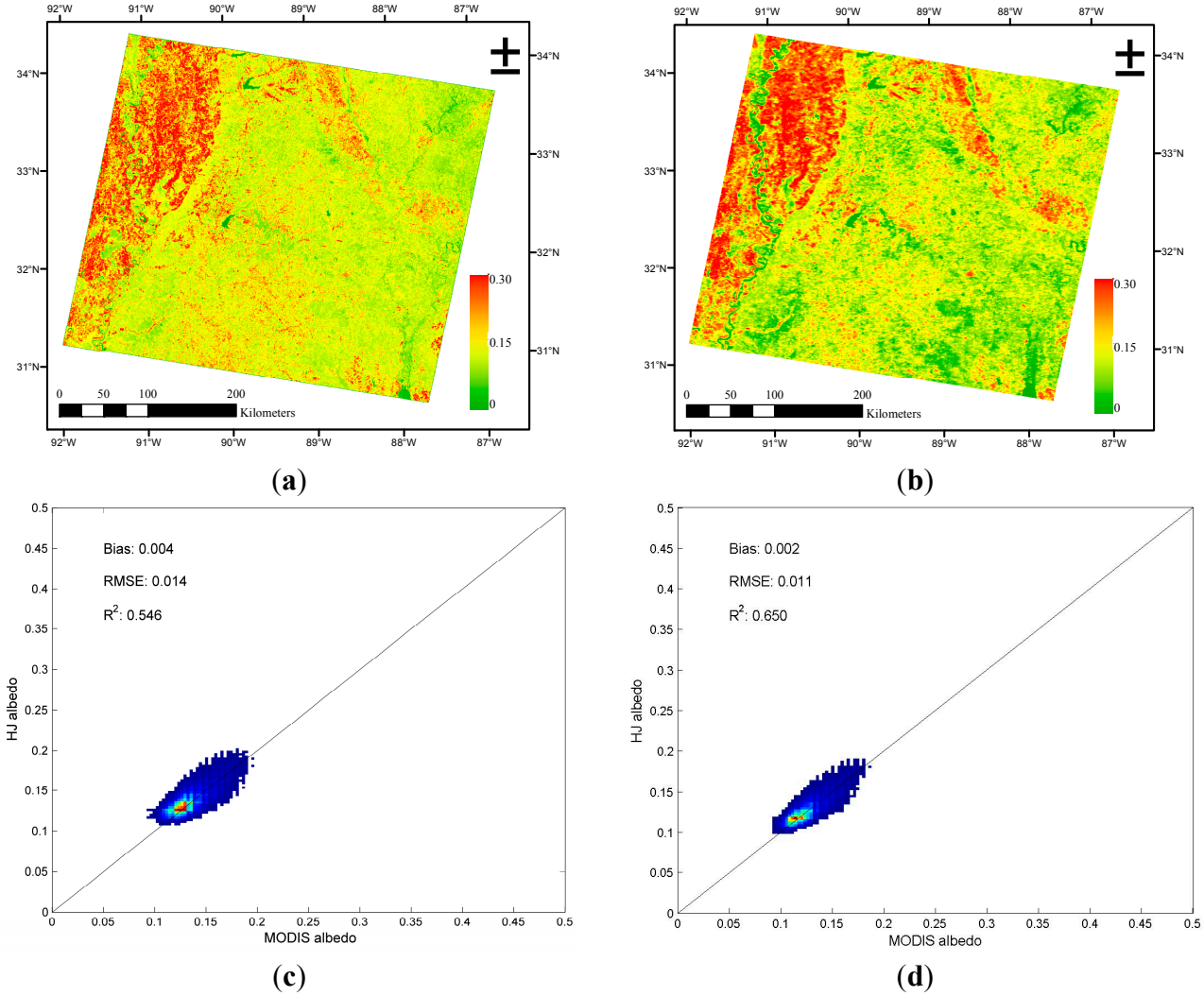

Figure 8. White-sky albedo maps from (**a**) HJ data and (**b**) MODIS 500 m albedo product; Scatter plots (density plot: low density in blue and high density in red) between HJ albedo and MODIS product for (**c**) white-sky albedo and (**d**) black-sky albedo in Mississippi, USA on 23 September 2014. Some water bodies are masked in white in the MODIS product.

The white-sky albedo maps from the two datasets (Figure 8a,b) show similar patterns of albedo spatial distribution in general, while much more detail of spatial variation can be found in the HJ albedo map. Figure 8c shows that the albedo derived from HJ data agrees well with the high-quality MODIS product, with a negligible bias of 0.004 and an RMSE of 0.014 (about 10.6% in relative value). The comparison of black-sky albedos (Figure 8d) shows improved results over that of white-sky albedos with a bias of 0.002, RMSE of 0.011, and R^2 of 0.650, which agrees well with the statistics shown in Figure 4 and suggests that with HJ's limited angular sampling the black-sky albedo is more accurate than white-sky albedo. Accompanied by the low signal-to-noise ratio (SNR), some significant striping noise is visible in part of the HJ data, which contributed to the errors found in the comparison. In addition, the adjacency

effects not considered in the spatial aggregation of HJ albedo to MODIS scale also led to some uncertainties in the comparison.

Among the same data shown in Figure 8, the albedo data for the forest pixels were extracted based on the land cover map from the National Land Cover Database 2011 (NLCD 2011) [38] and their relative albedo accuracies against MODIS products were plotted in Figure 9. The HJ albedo estimation generally improves by more than 5% as the view zenith angle increases, which is similar to the findings from the validation against ground measurements (see Figure 7). At the same time, the bias remains stable relative to the relative RMSE (RRMSE) in HJ albedo. The RRMSE keeps decreasing until the view zenith angle reaches 20°, although most of the decrease occurs when the view zenith angle becomes larger than 5°. Nevertheless, this demonstrates the unique advantage of wide-swath satellite data in capturing the surface BRDF information and thus the albedo estimation compared with nadir view satellite sensors.

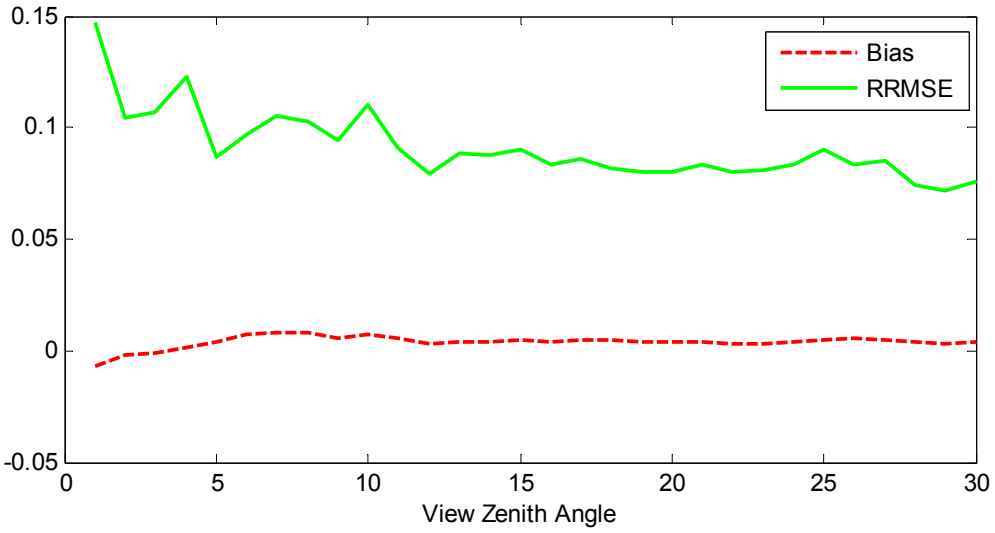

Figure 9. Relationship between HJ white-sky albedo estimation accuracy compared with MODIS product and view zenith angle for forest samples: bias and RRMSE. RRMSE is calculated as the ratio of absolute difference in HJ albedo and MODIS albedo to MODIS albedo.

4. Summary and Conclusions

This paper proposes an algorithm that directly estimates surface albedo from TOA observations acquired by HJ satellites by incorporating a MODIS-based surface BRDF database into the radiative transfer simulations to correct the angular effects. Validation against ground measurements shows that the proposed algorithm is capable of producing accurate surface albedo over both snow-free and snow-covered surfaces with an RMSE of 0.030, which suggests the feasibility of using HJ data for medium-resolution surface albedo monitoring and coarse-resolution data evaluation. Both validations against ground measurements and MODIS albedo products indicate that the accuracy of albedo estimation improves with an increase in view zenith angle as a result of the large field-of-view of HJ sensors, which further demonstrates the unique advantage of HJ data in the albedo estimation compared with other medium-resolution sensors.

Apart from the potential of using this algorithm for albedo monitoring over snow-covered surfaces, the uncertainties of snow-free albedo estimation from HJ data are slightly larger than those results from the Landsat data [22,23,26]. The limited spectral coverage of HJ sensors, its calibration accuracy, striping noise, and low SNR are likely the main factors causing the increased uncertainty in albedo estimation. In addition, the band conversion from MODIS to HJ data can lead to an error of 0.003–0.007. More efforts are needed to understand the pixel level difference between HJ albedo and MODIS products. Nevertheless, the inter-comparison of HJ albedo with MODIS product suggests that the proposed algorithm can still achieve a good accuracy in albedo estimation with an RMSE of 0.011–0.014 over a variety of land cover types even with the reduced spectral coverage and low SNR of HJ data.

In order to further improve the surface albedo estimation, refining the radiometric calibration is a possible solution. Alternatively, a usage of multi-angular observations, provided by the short revisiting periods (<4 days) of HJ data, would also significantly reduce the uncertainties through sampling the BRDF [35], which, however, was not implemented in this study due to lack of enough HJ data.

Based on the results using the wide-swath HJ data, we are confident that this approach can be revised and applied to other similar data sets, such as Landsat satellite series and the forthcoming Sentinel-2 satellites.

Acknowledgments

This work was supported by the NASA grant NNX09AN36G through the University of Maryland, College Park. We would like to thank the MODIS and HJ teams for maintaining the satellite data. Many thanks to the AmeriFlux PIs and SURFRAD teams for providing the ground measurements. We also thank the anonymous reviewers for their comments in improving the manuscript. We are grateful for the financial support from the University of Maryland Libraries Open Access Publishing Fund.

Author Contributions

Tao He, Shunlin Liang, and Dongdong Wang conceived and designed the experiments; Tao He performed the experiments and analyzed the data; Xiaona Chen and Dan-Xia Song conducted the manual georegistration of the HJ data; Bo Jiang helped download all the HJ data; and Tao He wrote the paper. All the authors reviewed and provided valuable comments for the manuscript.

Conflicts of Interest

The authors declare no conflict of interest.

References

1. Gaffin, S.R.; Imhoff, M.; Rosenzweig, C.; Khanbilvardi, R.; Pasqualini, A.; Kong, A.Y.Y.; Grillo, D.; Freed, A.; Hillel, D.; Hartung, E.; *et al*. Bright is the new black-multi-year performance of high-albedo roofs in an urban climate. *Environ. Res. Lett.* **2012**, *7*, doi:10.1088/1748-9326/7/1/014029.

2. Liang, S.L.; Zhang, X.; He, T.; Cheng, J.; Wang, D. Remote sensing of the land surface radiation budget. In *Remote Sensing of Energy Fluxes and Soil Moisture Content*; Petropoulos, G.P., Ed.; CRC Press: Boca Raton, FL, USA, 2013; pp. 125–165.
3. Wild, M.; Folini, D.; Schar, C.; Loeb, N.; Dutton, E.G.; Konig-Langlo, G. The global energy balance from a surface perspective. *Clim. Dyn.* **2013**, *40*, 3107–3134.
4. He, T.; Liang, S.L.; Song, D.X. Analysis of global land surface albedo climatology and spatial-temporal variation during 1981–2010 from multiple satellite products. *J. Geophys. Res.: Atmos.* **2014**, *119*, 10281–10298.
5. Liang, S.L.; Wang, K.C.; Zhang, X.T.; Wild, M. Review on estimation of land surface radiation and energy budgets from ground measurement, remote sensing and model simulations. *IEEE J. Sel. Top. Appl. Earth Obs. Remote Sens.* **2010**, *3*, 225–240.
6. Roman, M.O.; Gatebe, C.K.; Shuai, Y.; Wang, Z.; Gao, F.; Masek, J.G.; He, T.; Liang, S.; Schaaf, C.B. Use of *in situ* and airborne multiangle data to assess MODIS- and Landsat-based estimates of directional reflectance and albedo. *IEEE Trans. Geosci. Remote Sens.* **2013**, *51*, 1393–1404.
7. Roman, M.O.; Gatebe, C.K.; Schaaf, C.B.; Poudyal, R.; Wang, Z.S.; King, M.D. Variability in surface brdf at different spatial scales (30 m–500 m) over a mixed agricultural landscape as retrieved from airborne and satellite spectral measurements. *Remote Sens. Environ.* **2011**, *115*, 2184–2203.
8. Kuusinen, N.; Lukes, P.; Stenberg, P.; Levula, J.; Nikinmaa, E.; Berninger, F. Measured and modelled albedos in finnish boreal forest stands of different species, structure and understory. *Ecol. Model.* **2014**, *284*, 10–18.
9. Vanderhoof, M.; Williams, C.A.; Shuai, Y.; Jarvis, D.; Kulakowski, D.; Masek, J. Albedo-induced radiative forcing from mountain pine beetle outbreaks in forests, south-central rocky mountains: Magnitude, persistence, and relation to outbreak severity. *Biogeosciences* **2014**, *11*, 563–575.
10. Kuusinen, N.; Tomppo, E.; Shuai, Y.; Berninger, F. Effects of forest age on albedo in boreal forests estimated from MODIS and Landsat Albedo retrievals. *Remote Sens. Environ.* **2014**, *145*, 145–153.
11. Gao, F.; He, T.; Masek, J.G.; Shuai, Y.M.; Schaaf, C.B.; Wang, Z.S. Angular effects and correction for medium resolution sensors to support crop monitoring. *IEEE J. Sel. Top. Appl. Earth Obs. Remote Sens.* **2014**, *7*, 4480–4489.
12. Zhou, Y.Y.; Weng, Q.H.; Gurney, K.R.; Shuai, Y.M.; Hu, X.F. Estimation of the relationship between remotely sensed anthropogenic heat discharge and building energy use. *ISPRS J. Photogramm. Remote Sens.* **2012**, *67*, 65–72.
13. Roberts, D.A.; Quattrochi, D.A.; Hulley, G.C.; Hook, S.J.; Green, R.O. Synergies between vswir and tir data for the urban environment: An evaluation of the potential for the hyperspectral infrared imager (HYSPIRI) decadal survey mission. *Remote Sens. Environ.* **2012**, *117*, 83–101.
14. Jiang, B.; Liang, S.L.; Townshend, J.R.; Dodson, Z.M. Assessment of the radiometric performance of Chinese HJ-1 satellite ccd instruments. *IEEE J. Sel. Top. Appl. Earth Obs. Remote Sens.* **2013**, *6*, 840–850.
15. Wang, Z.; Xiao, P.F.; Gu, X.F.; Feng, X.Z.; Li, X.Y.; Gao, H.L.; Li, H.; Lin, J.T.; Zhang, X.L. Uncertainty analysis of cross-calibration for HJ-1 CCD camera. *Sci. China Technol. Sci.* **2013**, *56*, 713–723.

16. Zhang, X.; Zhao, X.; Liu, G.D.; Kang, Q.; Wu, D.H. Radioactive quality evaluation and cross validation of data from the HJ-1A/B satellites' CCD sensors. *Sensors* **2013**, *13*, 8564–8576.
17. Chen, W.; Cao, C.X.; He, Q.S.; Guo, H.D.; Zhang, H.; Li, R.Q.; Zheng, S.; Xu, M.; Gao, M.X.; Zhao, J.A.; *et al*. Quantitative estimation of the Shrub canopy LAI from atmosphere-corrected HJ-1 CCD data in MU US sandland. *Sci. China Earth Sci.* **2010**, *53*, 26–33.
18. Sun, L.; Sun, C.K.; Liu, Q.H.; Zhong, B. Aerosol optical depth retrieval by HJ-1/CCD supported by MODIS surface reflectance data. *Sci. China Earth Sci.* **2010**, *53*, 74–80.
19. Zhang, M.W.; Tang, J.W.; Dong, Q.; Duan, H.T.; Shen, Q. Atmospheric correction of HJ-1 CCD imagery over turbid lake waters. *Opt. Express* **2014**, *22*, 7906–7924.
20. Li, Y.J.; Xue, Y.; He, X.W.; Guang, J. High-resolution aerosol remote sensing retrieval over urban areas by synergetic use of HJ-1 CCD and MODIS data. *Atmos. Environ.* **2012**, *46*, 173–180.
21. Wu, H.; Liang, S.L.; Tong, L.; He, T.; Yu, Y. Bidirectional reflectance for multiple snow-covered land types from MISR products. *IEEE Geosci. Remote Sens. Lett.* **2012**, *9*, 994–998.
22. Shuai, Y.M.; Masek, J.G.; Gao, F.; Schaaf, C.B. An algorithm for the retrieval of 30-m snow-free Albedo from Landsat surface reflectance and MODIS BRDF. *Remote Sens. Environ.* **2011**, *115*, 2204–2216.
23. Shuai, Y.M.; Masek, J.G.; Gao, F.; Schaaf, C.B.; He, T. An approach for the long-term 30-m land surface snow-free albedo retrieval from historic landsat surface reflectance and MODIS-based *a priori* anisotropy knowledge. *Remote Sens. Environ.* **2014**, *152*, 467–479.
24. He, T.; Liang, S.L.; Wang, D.; Shi, Q.; Tao, X. Estimation of high-resolution land surface shortwave Albedo from Aviris data. *IEEE J. Sel. Top. Appl. Earth Obs. Remote Sens.* **2014**, *7*, 4919–4928.
25. Schaaf, C.B.; Gao, F.; Strahler, A.H.; Lucht, W.; Li, X.W.; Tsang, T.; Strugnell, N.C.; Zhang, X.Y.; Jin, Y.F.; Muller, J.P.; *et al*. First operational Brdf, Albedo Nadir reflectance products from MODIS. *Remote Sens. Environ.* **2002**, *83*, 135–148.
26. Franch, B.; Vermote, E.F.; Claverie, M. Intercomparison of landsat albedo retrieval techniques and evaluation against *in situ* measurements across the us surfrad network. *Remote Sens. Environ.* **2014**, *152*, 627–637.
27. Gao, B.; Jia, L.; Wang, T.X. Derivation of land surface albedo at high resolution by combining HJ-1A/B reflectance observations with MODIS BRDF products. *Remote Sens.* **2014**, *6*, 8966–8985.
28. He, T.; Liang, S.L.; Wang, D.; Wu, H.; Yu, Y.; Wang, J. Estimation of surface albedo and directional reflectance from moderate resolution imaging spectroradiometer (MODIS) observations. *Remote Sens. Environ.* **2012**, *119*, 286–300.
29. Wang, D.; Liang, S.L.; He, T.; Yu, Y. Direct estimation of land surface albedo from VIIRS data: Algorithm improvement and preliminary validation. *J. Geophys. Res.: Atmos.* **2013**, *118*, 12577–12586.
30. Lucht, W.; Schaaf, C.B.; Strahler, A.H. An algorithm for the retrieval of Albedo from space using semiempirical BRDF models. *IEEE Trans. Geosci. Remote Sens.* **2000**, *38*, 977–998.
31. He, T.; Liang, S.L.; Wang, D.; Shuai, Y.; Yu, Y. Fusion of satellite land surface albedo products across scales using a multiresolution tree method in the north central United States. *IEEE Trans. Geosci. Remote Sens.* **2014**, *52*, 3428–3439.

32. Wang, Z.S.; Schaaf, C.B.; Strahler, A.H.; Chopping, M.J.; Roman, M.O.; Shuai, Y.M.; Woodcock, C.E.; Hollinger, D.Y.; Fitzjarrald, D.R. Evaluation of MODIS Albedo product (MCD43A) over grassland, agriculture and forest surface types during dormant and snow-covered periods. *Remote Sens. Environ.* **2014**, *140*, 60–77.
33. Liang, S.L.; Strahler, A.H.; Walthall, C. Retrieval of land surface albedo from satellite observations: A simulation study. *J. Appl. Meteorol.* **1999**, *38*, 712–725.
34. Vermote, E.F.; Tanre, D.; Deuze, J.L.; Herman, M.; Morcrette, J.J. Second Simulation of the Satellite Signal in the Solar Spectrum, 6S: An overview. *IEEE Trans. Geosci. Remote Sens.* **1997**, *35*, 675–686.
35. He, T.; Liang, S.L.; Wang, D. Direct estimation of land surface Albedo from simultaneous multi-angle MISR data. *Remote Sens. Environ.* **2015**, submitted.
36. Wang, D.; Liang, S.L.; He, T.; Yu, Y.; Schaaf, C.; Wang, Z. Estimating daily mean land surface albedo from MODIS data. *J. Geophys. Res.: Atmos.* **2015**, submitted.
37. Cescatti, A.; Marcolla, B.; Vannan, S.K.S.; Pan, J.Y.; Roman, M.O.; Yang, X.Y.; Ciais, P.; Cook, R.B.; Law, B.E.; Matteucci, G.; *et al*. Intercomparison of MODIS albedo retrievals and *in situ* measurements across the global fluxnet network. *Remote Sens. Environ.* **2012**, *121*, 323–334.
38. Jin, S.M.; Yang, L.M.; Danielson, P.; Homer, C.; Fry, J.; Xian, G. A comprehensive change detection method for updating the national land cover database to *circa* 2011. *Remote Sens. Environ.* **2013**, *132*, 159–175.